scientific reports

OPEN

Theoretical investigation on BeN$_2$ monolayer for an efficient bifunctional water splitting catalyst

M. R. Ashwin Kishore[1], R. Varunaa[2], Amirhossein Bayani[1] & Karin Larsson[1]✉

The search for an active, stable, and abundant semiconductor-based bifunctional catalysts for solar hydrogen production will make a substantial impact on the sustainable development of the society that does not rely on fossil reserves. The photocatalytic water splitting mechanism on a BeN$_2$ monolayer has here been investigated by using state-of-the-art density functional theory calculations. For all possible reaction intermediates, the calculated changes in Gibbs free energy showed that the oxygen evolution reaction will occur at, and above, the potential of 2.06 V (against the NHE) as all elementary steps are exergonic. In the case of the hydrogen evolution reaction, a potential of 0.52 V, or above, was required to make the reaction take place spontaneously. Interestingly, the calculated valence band edge and conduction band edge positions for a BeN$_2$ monolayer are located at the potential of 2.60 V and 0.56 V, respectively. This indicates that the photo-generated holes in the valence band can oxidize water to oxygen, and the photo-generated electrons in the conduction band can spontaneously reduce water to hydrogen. Hence, the results from the present theoretical investigation show that the BeN$_2$ monolayer is an efficient bifunctional water-splitting catalyst, without the need for any co-catalyst.

Fossil resources, such as oil, gas, and coal are depleting rapidly, which urge the research community to find alternative energy technologies to be able to solve the demands of global energy issues. One of the promising alternative technologies is solar hydrogen production through water splitting with the help of semiconductors. The past few decades have seen tremendous efforts in the discovery and fabrication of highly efficient semi-conducting photocatalysts for water splitting, including metal oxides, metal sulfides, metal nitrides, and metal oxynitrides[1–5]. However, some of these materials suffer from poor absorption of solar light, and photo-corrosion. Therefore, finding an efficient photocatalyst for water splitting is still a challenging problem. At present, the best-known catalyst for oxygen evolution reaction (OER) and hydrogen evolution reaction (HER) is ruthenium oxides, iridium oxides, and platinum-based materials[6–9]. However, the scarcity and high cost of noble metals and precious metal oxides impose severe limitations for large-scale applications. The development of efficient and stable materials for OER and HER, by modifying chemical composition, structure, morphology, and support, is therefore of largest importance.

Two-dimensional (2D) materials have attracted increasing attention in numerous research fields during the past few years. This is owing to their superior properties, which are completely different from their bulk counter-parts. The prospect of using these 2D materials in the field of energy conversion and storage, is very promising due to their various intrinsic properties, such as the presence of many surface-active sites, enhanced electron-hole separation, fast mobility of photogenerated charge carriers, and reduced recombination rate. After the graphene's breakthrough, a wide range of 2D materials for HER and OER have been extensively examined[10–14]. Graphene-based materials, like N-doped graphene[15,16] and N-containing co-doped graphene[17], have been reported as excellent catalysts for HER and OER of high activity. Transition metal dichalcogenides (TMDs)[18,19], metal monochalcogenides[20], MXenes[21,22], g-C$_3$N$_4$[23,24], and C$_2$N[25–27], have also been identified as potential catalysts for water splitting.

The BeN$_2$ monolayer is a graphene-like honeycomb lattice with an optically active direct bandgap of 2.23 eV[28]. This is a theoretically predicted material that possesses high mechanical, thermal, and lattice dynamical stability. The reported carrier mobility at room temperature is higher than that of many other 2D materials[29–31]. All these exceptional properties make the BeN$_2$ monolayer very attractive for photocatalytic applications. Very few reports are available on this material for energy storage and conversion applications to date. Ding et al.[32]

[1]Department of Chemistry, Ångström Laboratory, Uppsala University, Box 538, 751 21 Uppsala, Sweden. [2]Department of Physics, Central University of Tamil Nadu, Thiruvarur, Tamil Nadu 610101, India. ✉email: karin.larsson@kemi.uu.se
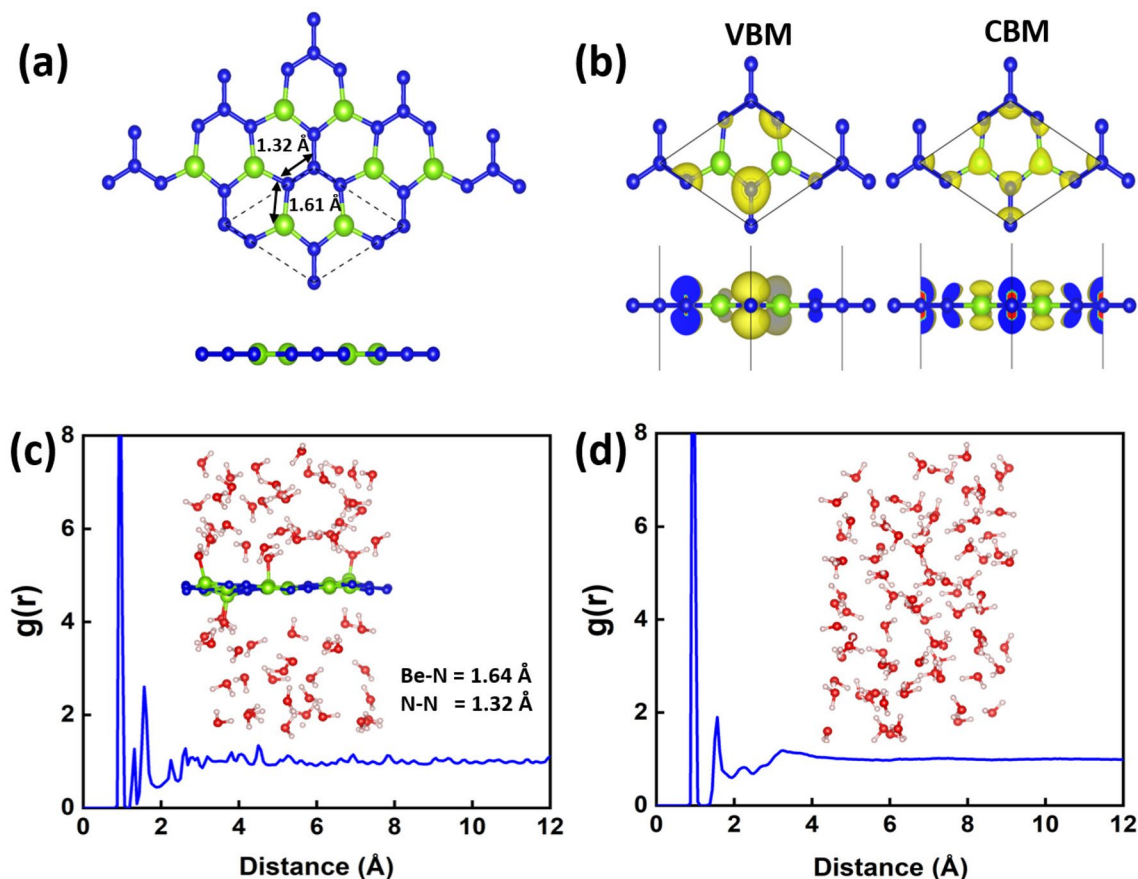
Figure 1. This figure shows some results for a monolayer of BeN₂: (**a**) Schematic geometrical structure in top and side views (the dashed lines indicate the unit cell); (**b**) Top and side views of isosurface plots of the charge densities at the VBM and CBM, respectively (the isosurface value is 0.008 e Å^{-3}); The normalized pair correlation functions g(r) of (**c**) BeN₂ monolayer in liquid water and (**d**) liquid water after annealing at 300 K for 5 ps. The inset in (**c**) shows the structural evolution of the BeN₂ in liquid water and average bond lengths of Be-N/N-N. The inset in (**d**) shows the structural evolution of water molecules after annealing at 300 K for 5 ps, respectively. Be, N, O, and H atoms are marked in green, blue, red, and beige, respectively.

elucidated the oxygen reduction reaction mechanism for the BeN₂ monolayer. It was found that the overpotential is 0.45 eV in an acidic environment, and with zero overpotential in an alkaline environment. Moreover, Wei et al.[33] studied the photocatalytic water splitting activity onto this monolayer through the band edge position with respect to the water redox potentials. However, the reaction mechanism for the catalysis of HER and OER have not yet been reported for this material.

The purpose with the present study has been to get a deeper understanding about the reaction mechanisms of HER and OER that takes place on a BeN₂ monolayer, and also to evaluate their overpotentials. These HER and OER catalytic processes have therefore been systematically investigated, using calculations based on the density functional theory (DFT). As a result, the calculated electronic properties, and band edge alignment, indeed show that the BeN₂ monolayer has the potential to function as a bifunctional catalyst in the splitting of water by using solar light. Moreover, the investigation of OER and HER mechanisms resulted in overpotentials of 0.83 V and 0.52 V (with reference to NHE), respectively. These very positive theoretical results indeed spread light on further experimental explorations.

Results and discussion

Structural and electronic properties. The optimized structure of the BeN₂ monolayer is shown in Fig. 1a. It possesses the P-62 M space group with a point group of D$_{3h}$. The calculated lattice constant (a=4.54 Å), bond lengths (Be−N = 1.61 Å ; N−N = 1.32 Å), and bond angles (Be−N−Be = 108.3° ; Be−N−N = 125.8°) are in accordance with previous reports[28,33]. Moreover, the band decomposed charge density, corresponding to the valence band maxima (VBM) and the conduction band minima (CBM) at the Γ point, is displayed in Fig. 1b. As can be seen in Fig. 1b, the charges at the VBM comprise the N-p$_z$ states, and that the charges at CBM arise from hybridization of both Be and N-p$_z$ states. The cohesive energy were calculated to evaluate the stability of the BeN₂. The cohesive energy is defined as:

$$E_{coh} = (nE_{Be} + 2nE_N - E_{BeN_2})/3n \tag{1}$$

where E_{Be}, E_N, and E_{BeN_2} are the total energy of single Be atom, single N atom and BeN$_2$ sheet, respectively. n is the number of formula unit in the BeN$_2$ cell. The calculated cohesive energy of BeN$_2$ is 5.03 eV/atom which is larger than other well known 2D materials such as silicene (4.57)[34], phosphorene (3.48)[35], and Al$_2$C sheet (4.58)[36]. This indicates the bonding in BeN$_2$ is strong and stable.

In order to gain more insight into the thermal and dynamical stability of the BeN$_2$ monolayer, analyses of phonon dispersion spectra, as well as of $ab-initio$ molecular dynamics simulations, have been performed. As shown in Fig. S1 (in the Supplementary file), it is evident that BeN$_2$ monolayer is dynamically stable since all vibration modes are real, and there are no imaginary frequency modes in the entire Brillouin zone. Moreover, the total potential energy fluctuation is minimum throughout the simulation period (as shown in Fig. S2). This indicates that the structure is not changed (with time) at room temperature. Also, the inset shows that the structure of the BeN$_2$ monolayer, at the end of the simulation, is planar with little buckling. It does not suffer drastic structural distortion or transformation, and, hence, this material is stable at room temperature.

It is also essential to investigate the stability of the BeN$_2$ monolayer in an aqueous environment. Therefore, the BeN$_2$ monolayer was placed in liquid water with a fixed density of 1 g cm^{-3} and annealed at 300 K for five pico-seconds. The calculated normalized pair correlation functions show some sharp peaks in the long-range part between 7 and 12 Å (see Fig. 1c), and this indicates that the BeN$_2$ monolayer remains crystalline after the annealing step in an aqueous environment. This is due to the fact that crystalline materials show long-range order features, and the amorphous materials show long range disorder features. The inset shows the structural evolution of the BeN$_2$ in liquid water, and is buckled due to interaction with water molecules. 2D materials usually show wrinkles at infinite temperatures, and these are reasons why the peaks are small. The calculated normalized pair correlation function for H$_2$O shown in Fig. 1d indicates the liquid nature of water, which is consistent with the XRD measurements[37].

Next, to evaluate the corrosion resistance or electrochemical stability of BeN$_2$, Pourbaix diagram is predicted. Figure S3 (in the supplementary information) shows the Pourbaix diagram of the BeN$_2$ system. An ionic concentration of 10^{-2} M for both Be and N species is used for the analysis. Materials with Gibbs free energy of decomposition $\Delta G_{pbx} = 0$ eV/atom are considered to be stable, whereas, for $\Delta G_{pbx} > 0$, they decompose to Pourbaix-stable phases in thermodynamic equilibrium. In general, materials which decompose to at least one solid phase might form a passivation layer on the surface to prevent further corrosion. As can be seen in Fig. S3, BeN$_2$ has a large window of thermodynamic stability in the whole alkaline region and some parts of the acidic region. However, at pH 0 in the redox region, the minimum of the ΔG_{pbx} is found to be 0.24 eV/atom. Earlier reports have shown that the well-known semiconducting materials such as GaP, Zn (FeO$_2$)$_2$, Si, WSe$_2$, GaAs, Fe$_2$O$_3$, WO$_3$, and TiO$_2$ are found to be stable experimentally, have a ΔG_{pbx} as high as 0.5 eV/atom. These materials are stable against corrosion due to self-passivation and formation of more stable solid-state surface phases[38]. Therefore, the BeN$_2$ at pH 0 can be considered to be stable in water through the development of a passivating film.

The electronic properties of the BeN$_2$ monolayer were evaluated by using band structure and density of states (DOS) analysis. The calculated band structure and DOS spectrum, using a GGA-PBE functional, are plotted in Fig. S3a. It is there shown that the BeN$_2$ monolayer is a direct bandgap semiconductor with a bandgap value of 1.34 eV at the Γ point. From the DOS spectrum it is clear that the VBM and CBM are originated from N-p states and hybridization with N and Be-p states, respectively. Be and P states are hybridized over the whole valence band, which indicates the presence of in-plane covalent bonding within the BeN$_2$ monolayer. The band structure of the BeN$_2$ monolayer, using the HSE06 functional (see Fig. S3b), was also calculated. The band dispersion is the same as that of PBE band structure, but the calculated HSE06 bandgap value is 2.26 eV. In general, the HSE06 functional improves the bandgap, but it has been shown that the single-shot $G_0 W_0$ calculation can provide an accurate estimation of the electronic bandgap in solids, which is close to experimental values. Therefore, the bandgap has there been calculated by using single-shot $G_0 W_0$ calculation, and the obtained bandgap value for the BeN$_2$ monolayer is 3.16 eV. This bandgap value was thereafter used to align the band edge positions with respect to water redox potentials (which will be discussed below).

Before investigating the OER and HER mechanisms, the adsorption of the reaction intermediates O, OH, OOH, H, H$_2$O, and H$_3$O$^+$ onto the BeN$_2$ surface was studied. To understand the charge transfer characteristics between the reaction intermediates and BeN$_2$ surface, the charge density difference $\Delta\rho(r)$ was calculated (see Eq. (1))

$$\Delta\rho(r) = \Delta\rho_{BeN_2+Mol(r)} - \Delta\rho_{BeN_2} - \Delta\rho_{Mol(r)} \tag{2}$$

where $\Delta\rho_{BeN_2+Mol(r)}$, $\Delta\rho_{BeN_2}$, and $\Delta\rho_{Mol(r)}$ are the charge densities of the adsorbed system, isolated BeN$_2$ sheet, and isolated molecule in adsorbing configuration, respectively. Bader's atoms-in-molecule approach is used to measure the charge being transferred quantitatively[39]. For the situation with an atomic O adsorbate, the oxygen atom was found to break the Be−N bond and form a chemical bond with both Be and N. As can be seen in Fig. 3b, the resulting bond lengths are 1.55 Å (Be−O) and 1.37 Å (O−N). These values can be understood from the calculated partial density of states (PDOS) (as displayed in Fig. 2a,b). For the BeN$_2$ monolayer, it is obvious that the VBM originates from N-p$_z$ and the CBM originates from N-p$_z$ (with a small contribution from Be-p$_z$). In addition, the p$_x$ and p$_y$ orbitals of the Be and N atoms are involved in forming the in-plane covalent bonds, which indicates that this specific material is sp^2 hybridized. Moreover, the weak N(p$_z$)-Be(p$_z$) overlap prone to react with the incoming O atom. It is evident from the PDOS of the O adsorbed system that the O atom will strongly bind with N and Be as their p-states are strongly hybridized near the Fermi level. Due to this circumstance, the Be and N atoms will buckle up from its xy−plane, which is a clear indication of a sp^3 bonding feature. Futhermore, it can be seen from the iso-surface of charge density difference plot, as shown in Fig. S4a, that the charges will
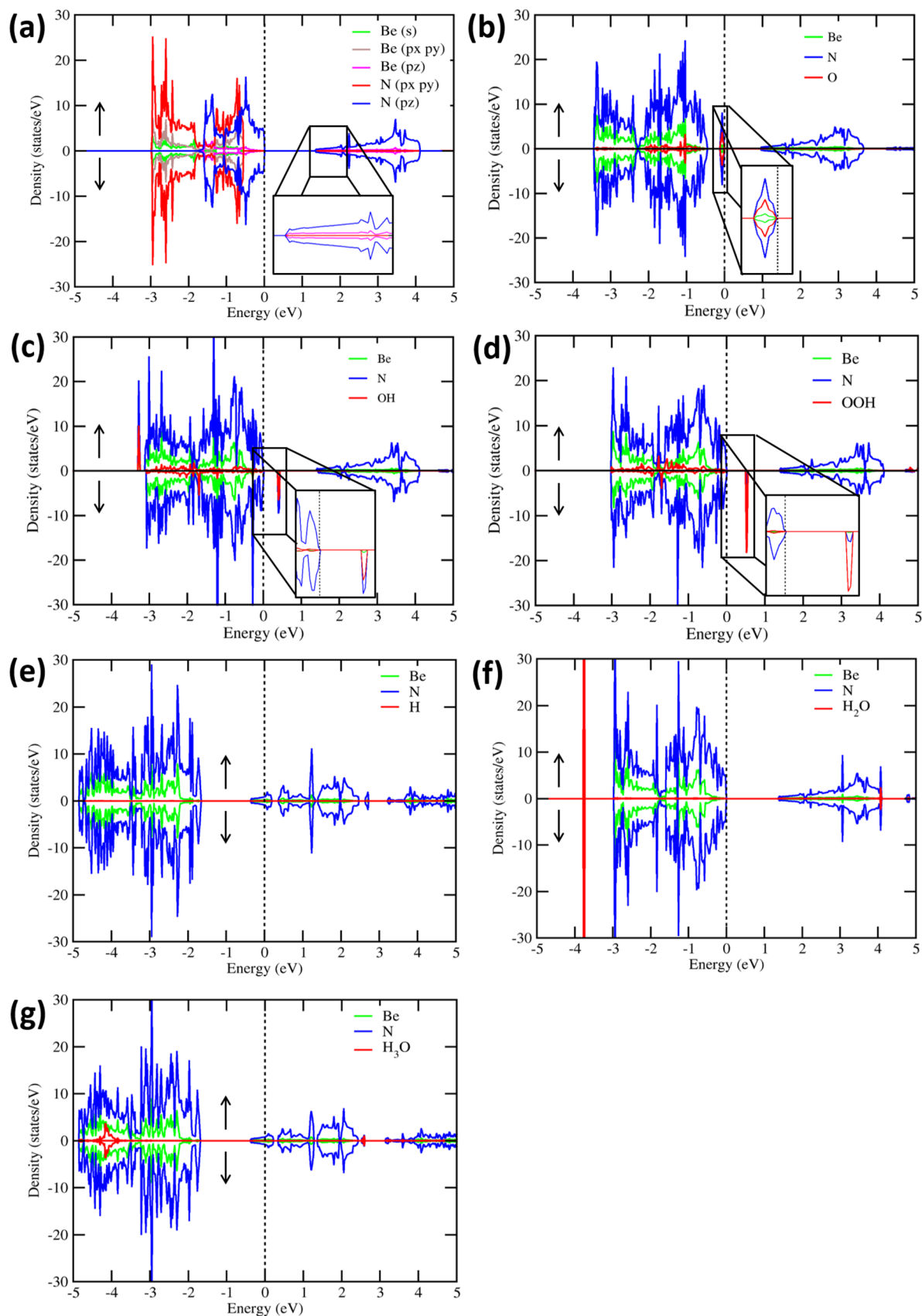
Figure 2. Calculated partial density of states for (**a**) a BeN$_2$ monolayer, and for the (**b**) O, (**c**) OH, (**d**) OOH, (**e**) H, (**f**) H$_2$O, and (**g**) H$_3$O adsorbates onto the BeN$_2$ monolayer. Arrows indicate the up (↑) and down (↓) spin channels. A magnified view of the states are shown in the insets.
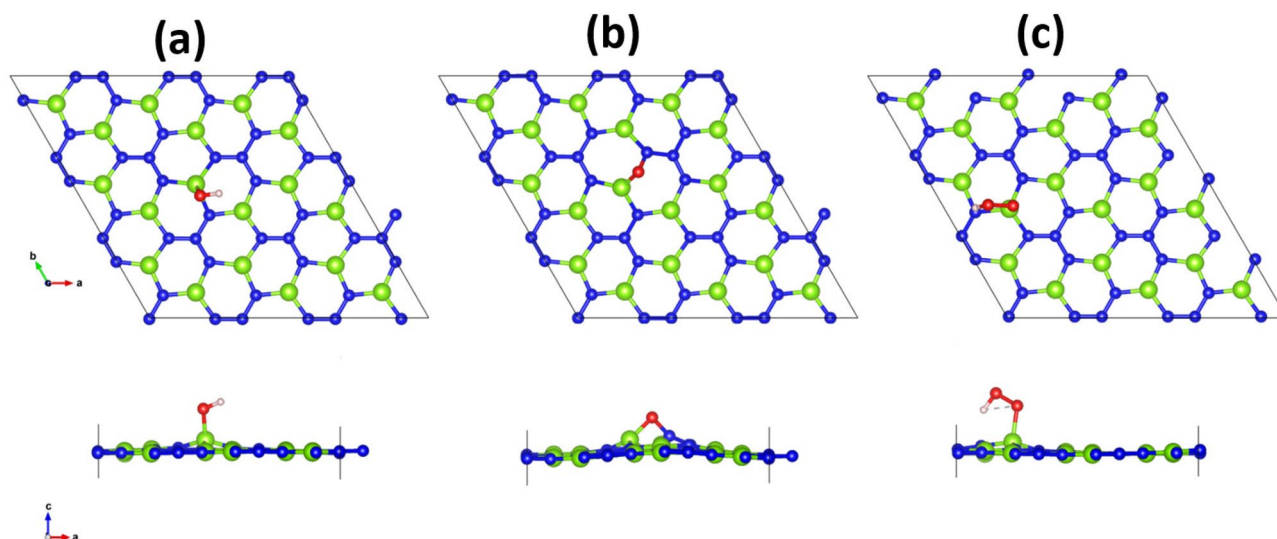
Figure 3. Optimized geometries of possible intermediates in the oxygen evolution reaction; (**a**) *OH, (**b**) *O, and (**c**) *OOH.

be transferred from the BeN_2 monolayer to the adsorbed O species. The Bader charge analysis indicated that the amount of charge transferred from the BeN_2 monolayer to the O species is 0.83 e.

For the situation with an OH adsorbate, it was shown to prefer to bind on top of the Be atom, and the Be–O bonding distance was found to be 1.63 Å . The Be atom is thereby somewhat buckled up from its xy−plane, indicating the occurrence of sp^3 hybridization. This has also earlier been observed for OH adsorption onto 2D boron-nitride and graphene[40]. Moreover, the OH adsorption also introduced unoccupied defect states in the bandgap region, as can be seen from the PDOS spectrum in Fig. 2c. These states were observed to be hybridized with the N/Be-p_z states in the valence band, which indicates a strong interaction between the OH radicals and the BeN_2 monolayer. In addition, the charge transfer analysis (see Fig. S4b) indicates that charges are depleted from BeN_2 monolayer and accumulated on the OH adsorbate. The following Bader charge analysis indicates that 0.53 e has been transferred upon OH adsorption.

As can be seen in Fig. 3c, OOH adsorbate prefers to bind on top of a surface Be atom, and the calculated bond lengths are 1.79 Å, 1.36 Å, and 1.03 Å for Be–O, O–O, and O–H, respectively. As was the situation with the OH adsorbate, the OOH adsorbate introduces unoccupied defect states in the bandgap region, and does also hybridize with N/Be-p_z states in the valence band (see Fig. 2d). Upon OOH adsorption, charges will be transferred from BeN_2 surface to OOH (as can be seen in Fig. S4c). The calculated Bader charge that OOH accepts is 0.27 e. From Bader analysis, it was found that the O adsorbate accepts more charges from BeN_2 layer than OH and OOH adsorbate. This is the reason why the adsorption energy is stronger for atomic O than OH and OOH adsorbate.

Atomic hydrogen was also observed to prefer to adsorb strongly onto N (in BeN_2), with an N–H bond length of 1.03 Å. As can be seen in the PDOS spectrum of the H-adsorbed system (see Fig. 2e), there are no hydrogen induced states within the bandgap. However, the Fermi level is shifted from a position within the bandgap to a position within the conduction band. This shift in Fermi level position is due to the well-known electron donor character of the atomic H. The charge transfer analysis confirms that there is a substantial depletion of electrons in the atomic H upon adsorption (see Fig. S4d). A Bader charge analysis reiterates that 0.44 e is depleted from H.

The H_2O molecule was shown to prefer an on top position of the Be atom in (BeN_2), with a distance of 1.94 Å. The PDOS spectrum displayed in Fig. 2f shows that the VBM and CBM of the BeN_2 monolayer are not significantly altered when H_2O is being adsorbed. However, there are H_2O induced states in valence band (VB) and in the conduction band (CB), and they are situated at −3.8 eV (VB) and at 4 eV (CB). A charge transfer analysis indicates that only a tiny amount of charge transfer occurs between the BeN_2 monolayer and the H_2O adsorbate (see Fig. S4e). Moreover, a Bader charge analysis shows that a net charge of 0.01 e is transferred from the BeN_2 monolayer to the H_2O adsorbate.

For the situation with H_3O^+, it was found to dissociatively adsorb onto the BeN_2 surface, forming a non-adsorbed H_2O molecule and an H adsorbate. The H atom will then chemically bind to the surface N atoms, and the water molecule will form a hydrogen bond with the H adsorbate (Fig. 5c). The PDOS spectrum of H_3O^+ adsorbed system is shown in Fig. 2g, displaying both the atomic H adsorption features, as well as the H_2O molecular feature. As such, the Fermi level is shifted from a position within the bandgap to a position within the conduction band, and there are H_2O induced states within the valence band at around − 4 eV. Moreover, Fig. S4f shows that the charges are redistributed between H_2O and atomic H, with a net charge of 0.49e being transferred to the BeN_2 monolayer (mainly from the adsorbed H species). The large transfer of charge from H to N (in BeN_2) will thereby induce a bond breakage within H_3O^+, leading to the two separate entities; molecular H_2O and the H adsorbate.

Band edge alignment. The band edge position with respect to water redox potentials is a crucial factor in determining whether a material is a potential photocatalyst or not. To facilitate the water redox reactions, the conduction band edge should be higher than water reduction potentials, whereas the valence band edge should be lower than water oxidation potential. The positions of VBM and CBM of the BeN_2 monolayer has here been determined by the bandgap center energy (E_{BGC}) and its bandgap (E_g) (see Eq. (2)).
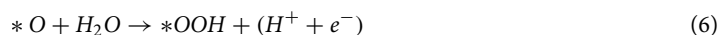
$$E_{CBM/VBM} = E_{BGC} \pm \frac{1}{2}E_g \qquad (3)$$

Since E_{BGC} has shown to be quite insensitive to the choice of exchange-correlation functional, we have used the less expensive PBE functional. The photoemission/inverse photoemission (PE/IPE) gap calculated with G_0W_0 was then used to obtain the CBM and VBM energy by adding and subtracting half of the PE/IPE gap from the E_{BGC}, respectively. The vacuum level was set to zero to align the energy levels for the BeN_2 monolayer.

The band edge potential diagram is plotted in Fig. S3c. From this figure, it is clear that the band edge positions of BeN_2 straddle the water redox potentials at pH 0, so this meets the thermodynamic requirement of an efficient photocatalyst to split water into hydrogen and oxygen. The CBM is located at 0.56 eV higher in energy than the reduction potential of H^+/H_2 (− 4.44 eV vs. the vacuum level), and the VBM is located at 1.37 eV lower in energy than the oxidation potential of O_2/H_2O (− 5.67 eV vs.the vacuum level). As the VBM is highly stabilized, it improves the hole transfer process to the redox species and this reduces the probability of charge carrier recombination, which in turn enhances the photocatalytic water splitting activity.

To evaluate the ability of electron-hole transfer, we calculated the effective masses of an electron and a hole along the Γ-K and Γ-X directions. Effective of electron and hole were derived from the band structure plot (see Fig. S3a) using the band fitting method. The second-order partial derivative of the valence band maxima and conduction band minima were calculated to obtain the hole effective mass and the electron effective mass, respectively. The calculated effective mass of an electron along Γ-K and Γ-X directions are 0.24 m_e and 0.29 m_e, respectively. Moreover, the calculated effective mass of a heavy-hole along the Γ-K and Γ-X directions are 1.81 m_e and 1.90 m_e, whereas the effective mass of a light-hole along the Γ-K and Γ-X directions are 0.27 m_e and 0.34 m_e, respectively. In order to have an excellent charge carrier mobility, the effective mass of charge carriers should be lower than 0.5 m_e, at least in one crystallographic direction[41]. In the BeN_2 monolayer, the effective masses of both the electron and light-hole along the Γ-K and Γ-X directions, are lower than 0.5 m_e. This indicates that the charge carriers would respond quickly, which results in improved carrier mobility. It is interesting to note that the more stabilized valence band edge, in addition to the lower effective mass of holes, will make the BeN_2 monolayer an excellent candidate for photocatalyst for water splitting.

Oxygen evolution reaction (OER). The oxygen evolution capabilities of BeN_2 has also been studied by using the calculated reaction free energies of all the possible intermediates. This particular half-reaction is more demanding as it involves four redox processes over a narrow potential range. It also involves the coupling of multiple protons and electrons transfers, and the formation of two oxygen–oxygen bonds. The OER reaction steps can be seen in Eqs. (3)–(6)[42,43]:

$$* + H_2O \rightarrow *OH + (H^+ + e^-) \qquad (4)$$

$$*OH \rightarrow *O + (H^+ + e^-) \qquad (5)$$

$$*O + H_2O \rightarrow *OOH + (H^+ + e^-) \qquad (6)$$

$$*OOH \rightarrow * + O_2 + (H^+ + e^-) \qquad (7)$$

where *X refers to species X (X = *OH, *O, and *OOH) adsorbed on the BeN_2 surface. We have considered all the possible adsorption sites for the OER intermediates on the BeN_2 surface and the site with the most negative adsorption energy are referred to as the most stable site, and that has been used for further analysis.

The water molecule adsorption on a BeN_2 surface is the very first step of an OER, and it is the fundamental requisite to start the reaction process. The first elementary reaction step of a water molecule adsorbed onto the BeN_2 surface is to convert to *OH (the *notation means that the species is adsorbed to the surface) by releasing one proton-electron pair ($H^+ + e^-$). As can be seen from Fig. 3a, the *OH molecule binds chemically onto the Be atom, with the adsorption energy of − 1.34 eV. The free energy change for this reaction step (3) was calculated to be + 2.05 eV. The next reaction step for the adsorbed OH molecule is to convert to *O by releasing another proton-electron pair. In this case, the oxygen atom breaks the Be–N bond and forms a chemical bond with both Be and N. The adsorption energy was found to be − 2.42 eV. The free energy change for this reaction step (4) was calculated to be + 0.58 eV. The third reaction step involves a second water molecule that interacts with the adsorbed O on the BeN_2 surface, forming an *OOH intermediate upon releasing the third electron-proton pair. The *OOH prefers to bind onto the Be atom with the adsorption energy of − 0.61 eV. The free energy change for this reaction process (5) was calculated to be + 2.06 eV. The final reaction in the OER mechanism is the adsorbed OOH onto the BeN_2 surface, which will release the oxygen gas by releasing the fourth proton-electron pair. The calculated free energy change for this reaction (6) was calculated to be − 0.24 eV.

The calculated reaction free energy profile, with different electrode potentials, is displayed in Fig. 4a. As can be seen in figure, all reaction steps are endergonic, with an exception of the final step, O_2 evolution, at U = 0 V (with a total free energy change of + 4.45 eV). The third reaction step, OOH* formation, is the rate-limiting step
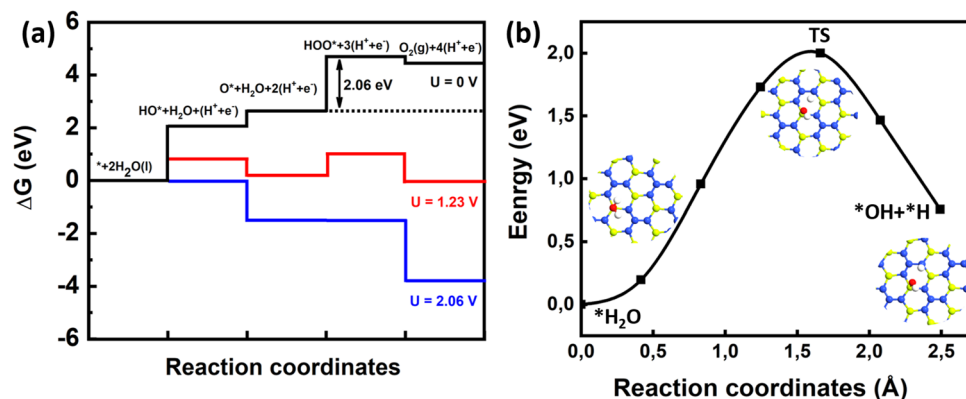
Figure 4. (**a**) Calculated free energy changes for the different intermediated reaction steps involved in the oxygen evolution reaction. (**b**) Minimum energy path for the dissociation of a water molecule into adsorbed OH and H species on a BeN_2 monolayer.

with a + 2.06 eV free energy change. At the equilibrium potential of 1.23 eV, two reaction steps were found to be endergonic, and two steps were exergonic. The *OH and *OOH formation reaction steps, where the proton is extracted from water, were uphill, whereas the O* and O_2 evolution reaction steps were downhill in nature. The free energy profile at U=2.06 V showed that all reaction steps were exergonic. Hence, the calculated OER overpotential (η^{OER}) became 0.83 V for BeN_2 monolayer. The holes in the valence band, with a potential of 2.06 eV and above, can thereby oxidize water to oxygen. Furthermore, the band edge alignment resulted in a location of the valence band edge at 2.60 eV, with respect to NHE. Therefore, the holes in the valence band of BeN_2 can oxidize water without any co-catalyst.

The first and third steps in the OER mechanism involves a proton extraction from water, and these two steps are more energy demanding than the other reaction steps. In order to estimate their associated barrier energies, the minimum energy path (MEP) for the dissociation of a water molecule into hydroxide and a proton were identified (i.e., where the proton becomes adsorbed onto BeN_2 surface instead to being transferred to the water medium) (see Eq. (7)).

$$*H_2O \rightarrow *OH + *H. \tag{8}$$

Figure 4b shows the MEP for the dissociation of a water molecule on the BeN_2 surface, along with the geometries of initial, final, and transition states. The calculated energy barrier for this dissociation reaction is 2 eV, which is lower than the free energy barriers of the first and third reaction steps in OER. Hence, the energy barrier does not affect the OER overpotential. It is very interesting that many photocatalysts can only satisfy HER, but not OER. However, here the presented results show that the BeN_2 monolayer is a promising catalyst for OER.

Hydrogen evolution reaction (HER). The hydrogen evolution reaction mechanism on the BeN_2 monolayer, has also been studied in the present investigation. Earlier studies have shown that the Gibbs free energy of hydrogen adsorption (ΔG_H^o) is the most important descriptor of HER activity[44,45]. If ΔG_H^o is close to zero, then the material will be a suitable catalyst for hydrogen evolution. The lower ΔG_H^o will results in a slow hydrogen release step (because of the strong bonds with hydrogen atoms), whereas higher ΔG_H^o will make the proton/electron-transfer step endothermal.

This reaction can proceed in two possible ways, either by hydrogen or by a water molecule. Both situations have here been looked at. The HER reaction steps are as follows (see Eqs. (8)–(11))[46–48]:

$$* + (H^+ + e^-) \rightarrow *H \tag{9}$$

$$*H + (H^+ + e^-) \rightarrow H_2 + * \tag{10}$$

HER can also proceed from the H_2O molecule

$$*H_2O + (H^+ + e^-) \rightarrow *H_3O \tag{11}$$

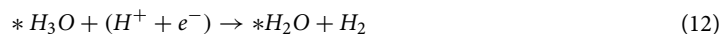$$*H_3O + (H^+ + e^-) \rightarrow *H_2O + H_2 \tag{12}$$

Figure 5a–c show the relaxed structures of HER intermediates *H, $*H_2O$, and $*H_3O$, respectively. It can be seen from this Figure that *H prefers to chemically bind on top of N atoms with the adsorption energy of 0.34 eV. The H_2O molecule prefers to physisorb on top of Be atom with an adsorption energy of − 0.24 eV. In the case of $*H_3O$, it was found to break into a water molecule and H. The adsorption energy was found to be − 0.075 eV. The calculated free energy profile is plotted in Fig. 6. It can be seen from this Figure that the adsorbed H requires higher reaction free energy than H_3O^+ adsorbate. Hence, the HER for the BeN_2 monolayer will proceed via H_3O^+
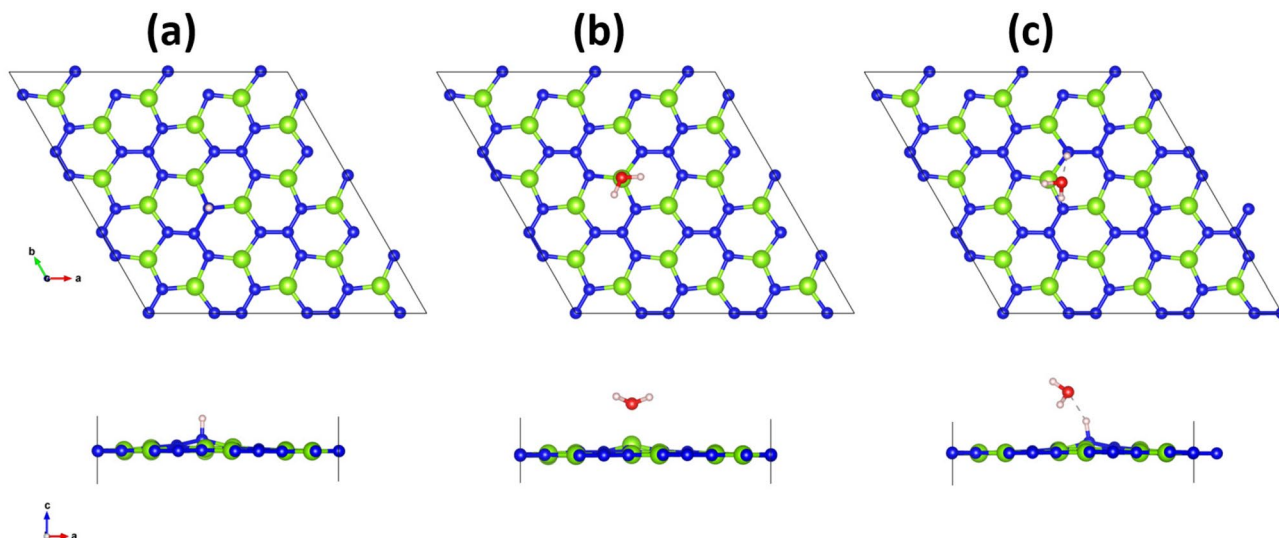
Figure 5. Optimized geometries of possible intermediates in the hydrogen evolution reaction; (**a**) *H, (**b**) *H_2O, and (**c**) *H_3O.
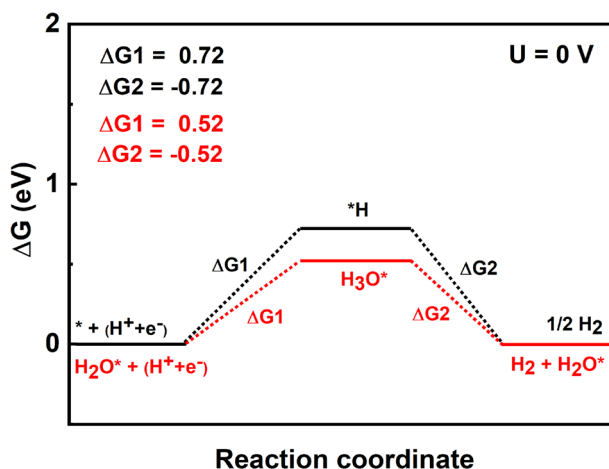

Figure 6. Calculated free energy changes of two suggested hydrogen evolution reaction; via H* formation (in black), or H_3O* formation (in red).

pathway instead of H pathway (in other words, it proceeds via an extra water molecule pathway). The calculated free energy is + 0.72 eV, which indicates that the overpotential for an overall H_2 evolution is − 0.72 V. When an extra water molecule is present, the free energy will decrease to + 0.52 eV, and the overpotential would thereby become − 0.52 V. From the band edge alignment, it was observed that the conduction band edge is located at 0.56 eV above the hydrogen reduction level. It is interesting to note that hydrogen evolution on the BeN_2 monolayer also proceeds without the aid of any co-catalyst.

Though OER and HER can spontaneously occur upon photoexcitation of the BeN_2 monolayer, the respective overpotential is not on par with some of the ideal OER and HER catalysts, like RuO_2[49,50], IrO_2[51], and Pt[52], etc. However, the BeN_2 monolayer is much better than other well-known catalysts, such as g-C_3N_4[53] (whose OER overpotential is very high). This material can only facilitate HER. g-CN is another example[54], which shows good activity for OER (but not HER). In addition, the CdS nanotube[55] has larger HER and OER overpotentials (as compared with the BeN_2 monolayer). The present state-of-the-art photocatalysts uses various surface engineering strategies or Z-scheme processes. The highest reported STH efficiency is 2.0% for a carbon dot loaded C_3N_4 (CDots-C_3N_4) photocatalyst[56]. This is a significant step in achieving the 5% STH target set by the US Department of Energy for photocatalysts in one-step water splitting.

Here, we compare the theoretically calculated band edge positions of BeN_2 with the experimentally measured band edge positions of CDots-C_3N_4. The CBM and VBM of CDots-C_3N_4 is positioned at 0.25 eV higher in energy than the reduction potential of H^+/H_2 (− 4.44 eV vs. the vacuum level), and 1.29 eV lower in energy than the oxidation potential of O_2/H_2O (− 5.67 eV vs. the vacuum level), respectively. In the case of BeN_2, the CBM is located at 0.56 eV higher in energy than the reduction potential, and the VBM is located at 1.37 eV lower in

energy than the oxidation potential, respectively. The VBM position of BeN_2 is comparable with that of CDots-$C_3 N_4$'s VBM, whereas CBM of BeN_2 is 0.25 eV higher than that of CDots-$C_3 N_4$'s CBM. In order to improve the photocatalytic activity of BeN_2, the CBM level should be shifted downward while slightly lowering or stabilizing the VBM. Also, the Gibbs free energy of HER and OER intermediates should be lowered.

In general, the adsorption strengths of the reaction intermediates (OH*, O*, and OOH*) strongly affect the catalytic activities. The adsorption strength should not be too strong, or too weak. Usually, in OER, the rate-determining step would be $O^* \rightarrow OOH^*$. This is also the case for the present BeN_2 system, and this is due to the larger adsorption energy of O* (−2.42 eV), as compared with OH* (−1.34 eV) and OOH* (−0.61 eV). The O atom strongly binds with Be and N atoms, which results in too strong O* adsorption. As the rate-limiting step in OER and HER is $O^* \rightarrow OOH^*$ and H*, one has to alter the electronic properties of the BeN_2 monolayer to weaken the adsorption strength of O* and H* (and thus tune the OER and HER activities, respectively). Therefore, chemical modification such as heteroatom doping, will introduce different kinds of defects. Oxidation, with the purpose to reduce the reaction overpotentials, will be required to significantly improve the electrocatalytic performances Research in this direction is in progress.

Conclusions

The reaction mechanism of the photocatalytic water splitting onto a BeN_2 monolayer has here been theoretically investigated by using density functional calculations. The calculated effective mass of electron and the hole indicate an excellent mobility in the lattice. This is a circumstance that improves the charge carrier separation, and, thus, reduces the recombination rate. In OER, it was found that the reaction step involving *OOH formation, was the rate-limiting step. In addition, the HER would proceed via the *H_3O pathway. The calculated overpotential for oxygen evolution and hydrogen evolution reaction is 0.83 V and 0.52 V (with reference to NHE), respectively. From band alignment with respect to water redox potentials, the results indicate that the photo-generated holes at the valence band can oxidize water to oxygen, and the photo-generated electrons at the conduction band can reduce water to hydrogen (without the aid of any co-catalyst). Hence, these results demonstrate that BeN_2 monolayer will act as a potential bifunctional catalyst that can reduce and oxidize water in the production of hydrogen.

Methods

All calculations were performed using the projector augmented wave (PAW) method, implemented in the *Vienna Ab initio Simulation Package* (VASP)[57]. The generalized gradient approximation proposed by Perdew, Burke, and Ernzrhof (GGA-PBE)[58] with van der Waals(vdW) correction proposed by Grimme, was used for the geometrical relaxation (due to its good description of long-range vdW interactions)[59]. Moreover, the Heyd-Scuseria-Ernzerhof (HSE06) hybrid functional was used in calculating the electronic structures (owing to the underestimation of semiconductor bandgaps when using the PBE functional)[60]. The Brillouin zone was sampled by using the Monkhorst-Pack scheme, with an employed **k**-mesh of $5 \times 5 \times 1$[61]. In addition, a plane-wave basis set, with a cutoff energy of 450 eV was used. A large vacuum of 18 Å was used to avoid spurious interactions. All structures were optimized until the total energy converged to less than 10^{-5} per atom, and the Helman-Feynman forces (that acting on each atom) was less than 0.01 eV/Å upon ionic relaxation. The postprocessing of the calculated data (using VASP) was done by using the VASPKIT code[62]. Moreover, the PHONOPY code was employed to calculate the phonon dispersion curves of the BeN_2 monolayer[63]. In addition, $ab-initio$ molecular dynamics (AIMD) simulations were used to evaluate the stability of the BeN_2 monolayer at 300 K. When studying the BeN_2 interface in vacuum, the simulations lasted for 10 ps, with a time step of 1 fs. For the BeN_2/water interface simulations, they lasted for 5 ps (with a time step of 0.5 fs). The Nosé algorithm[64] was used to control the temperature. The transition state was searched using the climbing image nudged elastic band (CI-NEB) method[65,66], as implemented in QuantumATK-2019.03.

Free energies for the intermediates in the oxygen evolution reaction (OER) and hydrogen evolution reaction (HER) have been computed by using the computational hydrogen electrode (CHE) model developed by Nørskov[46,47,67] and co-workers. By using this model, free energy changes of electrochemical reactions have been calculated by using the expression shown in Eq. (12)

$$\Delta G = \Delta E + \Delta ZPE - T\Delta S + \Delta G_U + \Delta G_{pH} \tag{13}$$

where ΔE, ΔZPE, and ΔS are the difference in DFT calculated total energy, zero-point energy, and entropy between final and initial states, respectively. The $\Delta G_U = -e$U, where U is the potential of the photogenerated electrons/holes with respect to the normal hydrogen electrode (NHE), and e is the number of transferred electrons. Here, $\Delta G_{pH} = 2.303 \, k_B$T pH, where kB is the Boltzmann constant, the temperature T has been taken as 300 K, and pH=0. Zero-point energy correction and entropies for adsorbed intermediates were calculated from vibrational frequencies analysis using density functional perturbation theory, whereas the entropies of the species in the gas phase were taken from the NIST database[68].

References

1. Ray, C. & Pal, T. Recent advances of metal-metal oxide nanocomposites and their tailored nanostructures in numerous catalytic applications. *J. Mater. Chem. A* **5**, 9465–9487 (2017).
2. Martha, S., Sahoo, P. C. & Parida, K. An overview on visible light responsive metal oxide based photocatalysts for hydrogen energy production. *Rsc Adv.* **5**, 61535–61553 (2015).

3. Chandrasekaran, S. *et al.* Recent advances in metal sulfides: from controlled fabrication to electrocatalytic, photocatalytic and photoelectrochemical water splitting and beyond. *Chem. Soc. Rev.* **48**, 4178–4280 (2019).
4. Han, N. *et al.* Recent advances in nanostructured metal nitrides for water splitting. *J. Mater. Chem. A* **6**, 19912–19933 (2018).
5. Ahmed, M. & Xinxin, G. A review of metal oxynitrides for photocatalysis. *Inorgan. Chem. Front.* **3**, 578–590 (2016).
6. Seitz, L. C. *et al.* A highly active and stable irox/sriro3 catalyst for the oxygen evolution reaction. *Science* **353**, 1011–1014 (2016).
7. Greeley, J. *et al.* Alloys of platinum and early transition metals as oxygen reduction electrocatalysts. *Nat. Chem.* **1**, 552 (2009).
8. Lim, B. *et al.* Pd-pt bimetallic nanodendrites with high activity for oxygen reduction. *science* **324**, 1302–1305 (2009).
9. Oezaslan, M., Hasche, F. & Strasser, P. Pt-based core-shell catalyst architectures for oxygen fuel cell electrodes. *J. Phys. Chem. Lett.* **4**, 3273–3291 (2013).
10. Yan, D. *et al.* Defect chemistry of nonprecious-metal electrocatalysts for oxygen reactions. *Adv. Mater.* **29**, 1606459 (2017).
11. Higgins, D., Zamani, P., Yu, A. & Chen, Z. The application of graphene and its composites in oxygen reduction electrocatalysis: a perspective and review of recent progress. *Energy Environ. Sci.* **9**, 357–390 (2016).
12. Deng, D. *et al.* Catalysis with two-dimensional materials and their heterostructures. *Nat. Nanotechnol.* **11**, 218 (2016).
13. Zhang, X., Chen, A., Zhang, Z., Jiao, M. & Zhou, Z. Transition metal anchored c 2 n monolayers as efficient bifunctional electro-catalysts for hydrogen and oxygen evolution reactions. *J. Mater. Chem. A* **6**, 11446–11452 (2018).
14. He, T., Matta, S. K., Will, G. & Du, A. Transition-metal single atoms anchored on graphdiyne as high-efficiency electrocatalysts for water splitting and oxygen reduction. *Small Methods* **3**(9), 1800419 (2019).
15. Yang, H. B. *et al.* Identification of catalytic sites for oxygen reduction and oxygen evolution in n-doped graphene materials: Development of highly efficient metal-free bifunctional electrocatalyst. *Sci. Adv.* **2**, e1501122 (2016).
16. Guo, D. *et al.* Active sites of nitrogen-doped carbon materials for oxygen reduction reaction clarified using model catalysts. *Science* **351**, 361–365 (2016).
17. Feng, Y. *et al.* Tuning the catalytic property of nitrogen-doped graphene for cathode oxygen reduction reaction. *Phys. Rev. B* **85**, 155454 (2012).
18. Chia, X., Eng, A. Y. S., Ambrosi, A., Tan, S. M. & Pumera, M. Electrochemistry of nanostructured layered transition-metal dichal-cogenides. *Chem. Rev.* **115**, 11941–11966 (2015).
19. Wang, F. *et al.* Recent advances in transition-metal dichalcogenide based nanomaterials for water splitting. *Nanoscale* **7**, 19764–19788 (2015).
20. Chowdhury, C., Karmakar, S. & Datta, A. Monolayer group iv–vi monochalcogenides: low-dimensional materials for photocatalytic water splitting. *J. Phys. Chem. C* **121**, 7615–7624 (2017).
21. Pang, J. *et al.* Applications of 2d mxenes in energy conversion and storage systems. *Chem. Soc. Rev.* **48**, 72–133 (2019).
22. Chaudhari, N. K. *et al.* Mxene: an emerging two-dimensional material for future energy conversion and storage applications. *J. Mater. Chem. A* **5**, 24564–24579 (2017).
23. Mishra, A. *et al.* Graphitic carbon nitride (g-c3n4)-based metal-free photocatalysts for water splitting: a review. *Carbon* **149**, 693–720 (2019).
24. Niu, W. & Yang, Y. Graphitic carbon nitride for electrochemical energy conversion and storage. *ACS Energy Lett.* **3**, 2796–2815 (2018).
25. Kishore, M. A. & Ravindran, P. Enhanced photocatalytic water splitting in a c2n monolayer by c-site isoelectronic substitution. *ChemPhysChem* **18**, 1526–1532 (2017).
26. Ashwin Kishore, M. & Ravindran, P. Tailoring the electronic band gap and band edge positions in the c2n monolayer by p and as substitution for photocatalytic water splitting. *J. Phys. Chem. C* **121**, 22216–22224 (2017).
27. Kishore, M. A., Sjåstad, A. O. & Ravindran, P. Influence of hydrogen and halogen adsorption on the photocatalytic water splitting activity of c2n monolayer: A first-principles study. *Carbon* **141**, 50–58 (2019).
28. Zhang, C. & Sun, Q. A honeycomb ben2 sheet with a desirable direct band gap and high carrier mobility. *J. Phys. Chem. Lett.* **7**, 2664–2670 (2016).
29. Yang, J.-H. *et al.* Two-dimensional sis layers with promising electronic and optoelectronic properties: theoretical prediction. *Nano Lett.* **16**, 1110–1117 (2016).
30. Xu, Y., Dai, J. & Zeng, X. C. Al2c monolayer sheet and nanoribbons with unique direction-dependent acoustic-phonon-limited carrier mobility and carrier polarity. *J. Phys. Chem. Lett.* **7**, 302–307 (2016).
31. Dai, J. & Zeng, X. C. Titanium trisulfide monolayer: theoretical prediction of a new direct-gap semiconductor with high and anisotropic carrier mobility. *Angew. Chem. Int. Ed.* **54**, 7572–7576 (2015).
32. Ding, Y.-M., Ji, Y., Dong, H., Rujisamphan, N. & Li, Y. Electronic properties and oxygen reduction reaction catalytic activity of h-ben2 and mgn2 by first-principles calculations. *Nanotechnology* **30**, 465202 (2019).
33. Wei, Y. *et al.* Promising photocatalysts for water splitting in ben2 and mgn2 monolayers. *J. Phys. Chem. C* **122**, 8102–8108 (2018).
34. Drummond, N., Zolyomi, V. & FalKo, V. Electrically tunable band gap in silicene. *Phys. Rev. B* **85**, 075423 (2012).
35. Vierimaa, V., Krasheninnikov, A. V. & Komsa, H.-P. Phosphorene under electron beam: from monolayer to one-dimensional chains. *Nanoscale* **8**, 7949–7957 (2016).
36. Li, Y., Liao, Y., von Ragué Schleyer, P. & Chen, Z. Al 2 c monolayer: the planar tetracoordinate carbon global minimum. *Nanoscale* **6**, 10784–10791 (2014).
37. Narten, A., Danford, M. & Levy, H. X-ray diffraction study of liquid water in the temperature range 4–200 c. *Discuss. Faraday Soc.* **43**, 97–107 (1967).
38. Singh, A. K. *et al.* Electrochemical stability of metastable materials. *Chem. Mater.* **29**, 10159–10167 (2017).
39. Yu, M. & Trinkle, D. R. Accurate and efficient algorithm for bader charge integration. *J. Chem. Phys.* **134**, 064111 (2011).
40. Grosjean, B. *et al.* Chemisorption of hydroxide on 2d materials from dft calculations: graphene versus hexagonal boron nitride. *J. Phys. Chem. Lett.* **7**, 4695–4700 (2016).
41. Le Bahers, T., Rérat, M. & Sautet, P. Semiconductors used in photovoltaic and photocatalytic devices: assessing fundamental properties from dft. *J. Phys. Chem. C* **118**, 5997–6008 (2014).
42. Valdes, A. & Kroes, G.-J. First principles study of the photo-oxidation of water on tungsten trioxide (wo 3). *J. Chem. Phys.* **130**, 114701 (2009).
43. Valdes, A., Qu, Z.-W., Kroes, G.-J., Rossmeisl, J. & Nørskov, J. K. Oxidation and photo-oxidation of water on TiO2 surface. *J. Phys. Chem. C* **112**, 9872–9879 (2008).
44. Hinnemann, B. *et al.* Biomimetic hydrogen evolution: MoS2 nanoparticles as catalyst for hydrogen evolution. *J. Am. Chem. Soc.* **127**, 5308–5309 (2005).
45. Skúlason, E. *et al.* Modeling the electrochemical hydrogen oxidation and evolution reactions on the basis of density functional theory calculations. *J. Phys. Chem. C* **114**, 18182–18197 (2010).
46. Rossmeisl, J., Logadottir, A. & Nørskov, J. K. Electrolysis of water on (oxidized) metal surfaces. *Chem. Phys.* **319**, 178–184 (2005).
47. Rossmeisl, J., Qu, Z.-W., Zhu, H., Kroes, G.-J. & Nørskov, J. K. Electrolysis of water on oxide surfaces. *J. Electroanal. Chem.* **607**, 83–89 (2007).
48. Wirth, J., Monturet, S., Klamroth, T. & Saalfrank, P. Adsorption and (photo-) electrochemical splitting of water on rutile ruthenium dioxide. *EPL* **93**, 68001 (2011).
49. Dickens, C. F. & Nørskov, J. K. A theoretical investigation into the role of surface defects for oxygen evolution on RuO2. *J. Phys. Chem. C* **121**, 18516–18524 (2017).

50. Roy, C. *et al.* Trends in activity and dissolution on ruo2 under oxygen evolution conditions: particles versus well-defined extended surfaces. *ACS Energy Lett.* **3**, 2045–2051 (2018).
51. Man, I. C. *et al.* Universality in oxygen evolution electrocatalysis on oxide surfaces. *ChemCatChem* **3**, 1159–1165 (2011).
52. Nørskov, J. K. *et al.* Trends in the exchange current for hydrogen evolution. *J. Electrochem. Soc.* **152**, J23–J26 (2005).
53. Wirth, J., Neumann, R., Antonietti, M. & Saalfrank, P. Adsorption and photocatalytic splitting of water on graphitic carbon nitride: a combined first principles and semiempirical study. *Phys. Chem. Chem. Phys.* **16**, 15917–15926 (2014).
54. Srinivasu, K. & Ghosh, S. K. Photocatalytic splitting of water on s-triazine based graphitic carbon nitride: an ab initio investigation. *J. Mater. Chem. A* **3**, 23011–23016 (2015).
55. Garg, P., Bhauriyal, P., Mahata, A., Rawat, K. S. & Pathak, B. Role of dimensionality for photocatalytic water splitting: CdS nanotube versus bulk structure. *ChemPhysChem* **20**, 383–391 (2019).
56. Liu, J. *et al.* Metal-free efficient photocatalyst for stable visible water splitting via a two-electron pathway. *Science* **347**, 970–974 (2015).
57. Kresse, G. & Furthmüller, J. Efficiency of ab-initio total energy calculations for metals and semiconductors using a plane-wave basis set. *Comp. Mater. Sci.* **6**, 15–50 (1996).
58. Perdew, J., Burke, K. & Ernzerhof, M. Generalized gradient approximation made simple. *Phys. Rev. Lett.* **78**, 1396 (1996).
59. Grimme, S. Semiempirical gga-type density functional constructed with a long-range dispersion correction. *J. Comput. Chem.* **27**, 1787–1799 (2006).
60. Heyd, J., Scuseria, G. E. & Ernzerhof, M. Hybrid functionals based on a screened coulomb potential. *J. Chem. Phys.* **118**, 8207–8215 (2003).
61. Monkhorst, H. J. & Pack, J. D. Special points for brillouin-zone integrations. *Phys. Rev. B* **13**, 5188 (1976).
62. Wang, V. Vaspkit, a post-processing program for the vasp code. https://vaspkit.sourceforge.net (2013).
63. Togo, A. & Tanaka, I. First principles phonon calculations in materials science. *Scr. Mater.* **108**, 1–5 (2015).
64. Shuichi, N. Constant temperature molecular dynamics methods. *Prog. Theor. Phys. Suppl.* **103**, 1–46 (1991).
65. Henkelman, G., Uberuaga, B. P. & Jónsson, H. A climbing image nudged elastic band method for finding saddle points and minimum energy paths. *J. Chem. Phys.* **113**, 9901–9904 (2000).
66. Smidstrup, S., Pedersen, A., Stokbro, K. & Jónsson, H. Improved initial guess for minimum energy path calculations. *J. Chem. Phys.* **140**, 214106 (2014).
67. Nørskov, J. K. *et al.* Origin of the overpotential for oxygen reduction at a fuel-cell cathode. *J. Phys. Chem. B* **108**, 17886–17892 (2004).
68. NIST databse. http://cccbdb.nist.gov/.

Acknowledgements

Author contributions

M.R.A.K conceptualized the research theme, performed the calculations, and wrote the manuscript. R.V and A.B took part in the data analysis. K.L. supervised the study. All authors reviewed the final manuscript.

Funding

Competing interests

The authors declare no competing interests.

Additional information

Supplementary information is available for this paper at https://doi.org/10.1038/s41598-020-77999-8.

Correspondence and requests for materials should be addressed to K.L.

Reprints and permissions information is available at www.nature.com/reprints.

Publisher's note Springer Nature remains neutral with regard to jurisdictional claims in published maps and institutional affiliations.